International Forum on Aeroelasticity and Structural Dynamics
IFASD 2022
June 13-17, 2022, Madrid, Spain

# TRANSITION FROM PRELIMINARY TO DETAILED DESIGN OF A HIGHLY ELASTIC SOLAR ELECTRIC AIRCRAFT

**Arne Voß[1], Christopher Koch[1], Steffen Niemann[2], Marius Mantei[2], Vega Handojo[1], Christian Weiser[3]**

[1] DLR - German Aerospace Center
Institute of Aeroelasticity
Bunsenstr. 10, 37073 Göttingen, Germany
arne.voss@dlr.de, christopher.koch@dlr.de, vega.handojo@dlr.de,

[2] DLR - German Aerospace Center
Institute of Composite Structures and Adaptive Systems
Lilienthalplatz 7, 38108 Braunschweig, Germany
steffen.niemann@dlr.de, marius.mantei@dlr.de

[3] DLR - German Aerospace Center
Institute of System Dynamics and Control
Münchener Straße 20, 82234 Weßling, Germany
christian.weiser@dlr.de

**Keywords:** High altitude platform, HALE, loads analysis, aeroelasticity, structural dynamics, structural sizing, flutter, preliminary design, detailed design

**Abstract:** This work presents the evolution of the aeroelastic modeling of a solar electric aircraft. The dimensions (wing span of ≈27.0 m) and the extreme light-weight construction (wing loading ≈4.0 kg/m²) results in a highly flexible aircraft, making aeroelastic analyses mandatory in all stages of the aircraft design. Comparing the preliminary with the detailed design phase, the aeroelastic models are significantly improved in their level of detail. Still, the models show similar structural dynamic characteristics and a comparable loading, e.g. in terms of wing bending and torsional moments $M_x$ and $M_y$, where the highest loads are caused by similar load cases. For the sizing, the analytic approach from the preliminary design is backed-up with numerical analyses using a detailed FE model. A comprehensive flutter analysis confirms the findings obtained from a flutter check during the preliminary design. Finally, first structural tests are prepared to validate the models.

## 1 MOTIVATION AND INTRODUCTION

The High Altitude Platform (HAP) is a very light weight, high altitude and long endurance aircraft (HALE) designed to stay airborne and hold position for several days at an altitude between FL450 and FL800 (≈14 to 24 km, above normal air traffic). Carrying optical

Figure 1: Early artist impression of the High Altitude Platform (HAP)

measurement equipment (up to 5.0 kg), this allows scientists to make observations of the earth continuously for a long period of time. This is an advantage compared to satellites, which typically pass the same spot only every couple of days and fly much higher, leading e.g. to a lower optical resolution. The ability to take-off and land allows to re-configure and re-locate the aircraft for new and different missions. In addition, purchase and operation costs of an aircraft are expected to be much lower compared to those of a satellite, including the infrastructure (airfield vs. spaceport). An illustration of the HAP configuration, currently under development at the DLR, is shown in Figure 1. The idea is to create a flight vehicle that flies very slow ($V_{\mathrm{EAS}}$ = 9.0 … 11.0 m/s) but is highly efficient in terms of propulsion and aerodynamic performance ($AR$ = 20) and is powered by solar electric energy. This requires a design which offers large areas for the installation of solar panels ($b_{ref}$ = 27.0 m) and is very light weight ( $m_{\mathrm{design}}$ = 136 kg) at the same time. During the night, the altitude is decreased and batteries are used, which are then re-charged during daytime while the aircraft re-gains altitude. Similar configurations, which are currently under development in the industry, are the Airbus Zephyr [1,9] (formerly developed by QinetiQ) or the Phasa-35 [12] by BAE Systems. Other comparable aircraft with and without a tailplane are the Solar Impulse [13] or the NASA Helios prototype [3]. The first two examples are planned for commercial use while the latter have a more scientific background.

During the progress of the project, the aircraft design has evolved and matured (from version HAP-O2 presented in [16]) to the current design (version HAP-O6 presented in [17]). On the one hand, more analyses have been performed, leading to a better knowledge and understanding of the configurations. On the other hand, the underlying data has improved, e.g. estimates of system masses have been replaced by the actual masses of the real components. Finally, the design became more detailed from a construction point of view (detailed CAD design of parts, drawings, manufacturing of prototypes, etc.), leading to more reliable mass and stiffness properties. In the first publication [16], the authors focused on a literature study of other HALE configurations and the selection of appropriate methods and tools to capture the anticipated aeroelastic effects. In the second publication [17], a large number of results were presented, ranging from a comprehensive loads analysis, including maneuver, closed-loop gust, landing and propulsion loads, the structural sizing and aeroelastic analysis,

including control surface effectiveness, longitudinal stability, a flutter check and the interaction of elastic modes with flight mechanics.

At the current stage, the configuration is nearly fixed, changes are expected only on the system side, e.g. the location of the battery packs will be optimized. This paper shows the transition from the preliminary to the detailed design phase and is structured as follows. Section 2 presents the evolution of the aeroelastic modeling. With this basis, Section 3 gives an overview on the selected load cases and the sizing and compares results obtained with the preliminary and the detailed models. Based on the detailed model, a comprehensive flutter analysis is performed in Section 4. Because the detailed models need a validation, Section 5 gives a preview on planned and ongoing tests. A summary and an outlook on further activities planned on the road towards the first flight are given in Section 6.

## 2 AEROELASTIC MODELING

This Section shows the transition from the modeling used in the preliminary design to a more detailed design. As mentioned in the introduction, the data from which the aeroelastic models are derived has improved, e.g. estimates of system masses have been replaced by the actual masses of the real components. Also, the design became more detailed from a construction point of view (detailed CAD design of parts, drawings, manufacturing of prototypes, etc.), leading to more reliable mass and stiffness properties.

Considering that there is a strong interaction of aeroelasticity with nearly all aspects of the aircraft design, this aircraft can be called “highly elastic”. However, this doesn't mean extreme geometric deformations, for example the wing tip deflection in horizontal level flight at normal operational speed is ≈5 … 6 % of the half-wing span. It can be concluded that the assumption of linearity still holds true and even for a pull-up maneuver, deflections of ≤ 15 % are calculated, thus geometrically nonlinear effects [10] are still small and negligible.

### 2.1 Structural Modeling

Because of the slender, beam-like structure of the configuration, mainly beam and bar elements are used to model the structure. The element stiffness and material characteristics are provided by the DLR Institute of Composite Structures and Adaptive Systems and are converted to a MSC.Nastran model using a combination of the parameterized model generator ModGen [7] and Excel. The preliminary beam model is shown in Figure 3 on the left and consists of the main spars and the fuselage beam. The more detailed model, shown in Figure 3 on the right, still uses beam elements but multiple details have been added, compare with the close-up in Figure 2. For the inboard wing section, ribs are modeled using four beam elements in chord direction and per rib. Two different types are considered: a normal rib and a reinforced rib where the ailerons are attached. The ailerons themselves are very long and slender (2.8 m in span direction and 0.2 m in chord direction) so that their bending and torsional properties might become important, especially because there is only one actuator. Their stiffness properties are modeled using beam elements as well. In the simulation, the deflections of the ailerons and the ribs under load are clearly visible, but the amplitudes remain small and have no significant effect on the overall aircraft, for example in terms of aeroelastic control surface effectiveness. The wing structure is covered with a foil-type skin and the additional stiffness was considered negligible at the beginning. Because the Young's

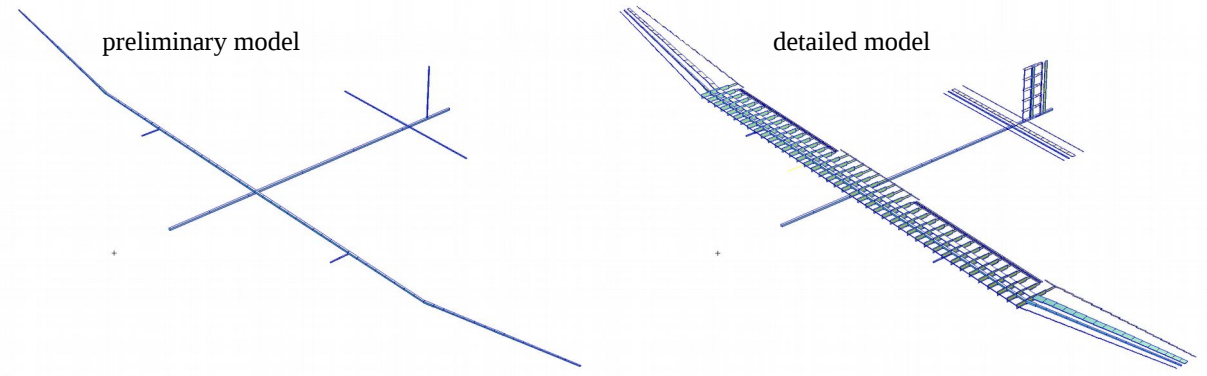


Figure 3: MSC.Nastran beam models, preliminary and more detailed model

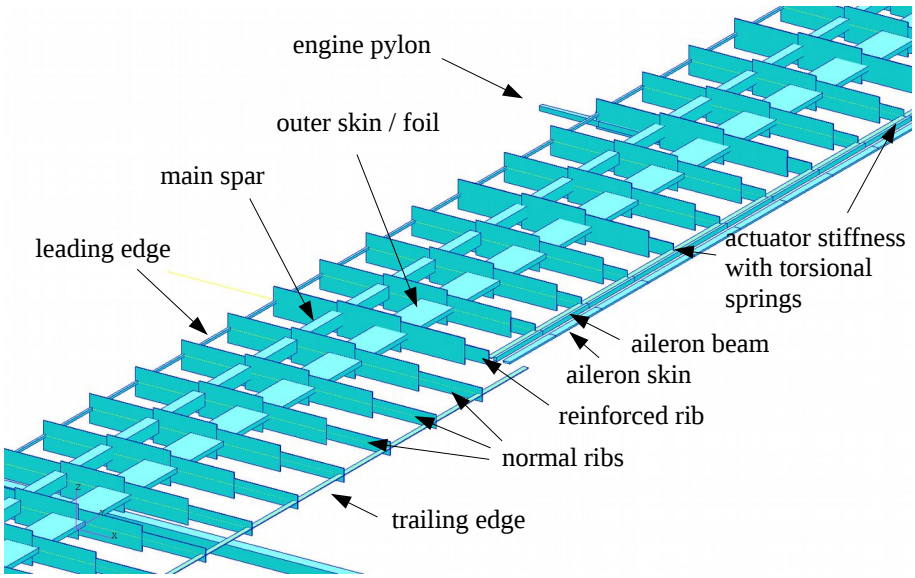


Figure 2: Close-up view on the beam elements of the inner wing, visualized using the area moments $I_{1,2}$

modulus is very low (≈2...3 GPa) and the foil is very thin (≈30...40 µm), this assumption is true for the out-of-plane bending stiffness. However, the skin's area moment $I_2$ (in-plane bending) is several times higher compared to $I_1$ (out-of-plane bending) and in addition, the skin has a significant impact on the torsional constant $J$. Especially for the outer wing where the torsional stiffness of the main spar decreases, the foil is calculated to contribute up to 50% to the wing torsional stiffness. To validate the modeling, currently a wing bending and torsion test and aileron tests are planned and described in Section 5.

The stiffness properties of the structural model are then extracted from MSC.Nastran (stiffness matrix $\mathbf{K}_{gg}$) and used in the DLR in-house loads and aeroelastic analysis software Loads Kernel [15].

### 2.2 Mass Modeling

Structural masses are derived from the element dimensions combined with material thickness and density, and are complemented by the system masses, which are provided by the DLR Institute of Flight Systems. All masses are attached as concentrated masses (CONM2) to the closest structural grid points. Note that the structural and mass models are treated separately because some structural members (e.g. joints, adhesives, mountings, etc.) are not included in the beam model but should be accounted for in the mass model.

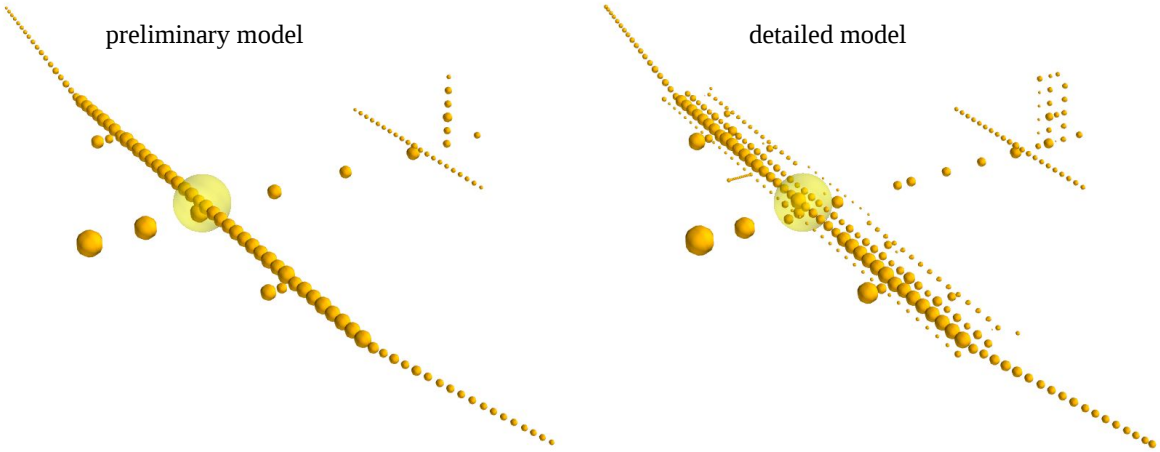


Figure 4: Mass discretization, preliminary and more detailed model

The mass discretization is shown in Figure 4 and the volume of the yellow spheres is proportional to the mass they represent and the large, transparent sphere indicates the center of gravity. There is a clear increase in the granularity between the preliminary and the more detailed model while the total mass ($\approx 136\ kg$) and the center of gravity stayed nearly constant. For most system masses, preliminary estimates were replaced by the actual masses and the actual location of installation and even the wiring and plug are now included. The secondary structural mass was smeared into the primary structure and is now modeled individually. This is an important step, for example the improved modeling of masses in chord direction leads to a more reliable calculation of the wing torsional frequencies.

Like the stiffness properties, the mass properties are extracted from MSC.Nastran (mass matrices $\mathbf{M}_{gg}$) as well.

### 2.3 Structural Dynamics

The eigenforms and -frequencies characterize the structural dynamic behavior of an aircraft and are important for aeroelastic analyses. Figure 5 shows the lowest frequency flexible mode shapes, calculated for the unconstrained aircraft in vacuum. Comparing the preliminary and the more detailed modeling, the frequency of the first wing bending, stayed nearly constant at 1.3 Hz. The frequency of the first in-plane wing bending used to coincide with the first wing bending for the preliminary model, which can be explained by the tube-type spar, which has the same stiffness properties in all directions. This behavior changed with the structural modeling of the leading and trailing edge. The third flexible mode is a combination of in-plane fuselage bending plus anti-symmetric wing bending. In the detailed model, this mode is now in second place and has a slight increase in frequency from 1.7 Hz to 2.0 Hz, indicating a stiffer fuselage.

The modes presented in Figure 5 are intended as an example, in the aeroelastic analyses up to 50 modes are included, which corresponds to frequencies of up to ≈ 45 Hz.

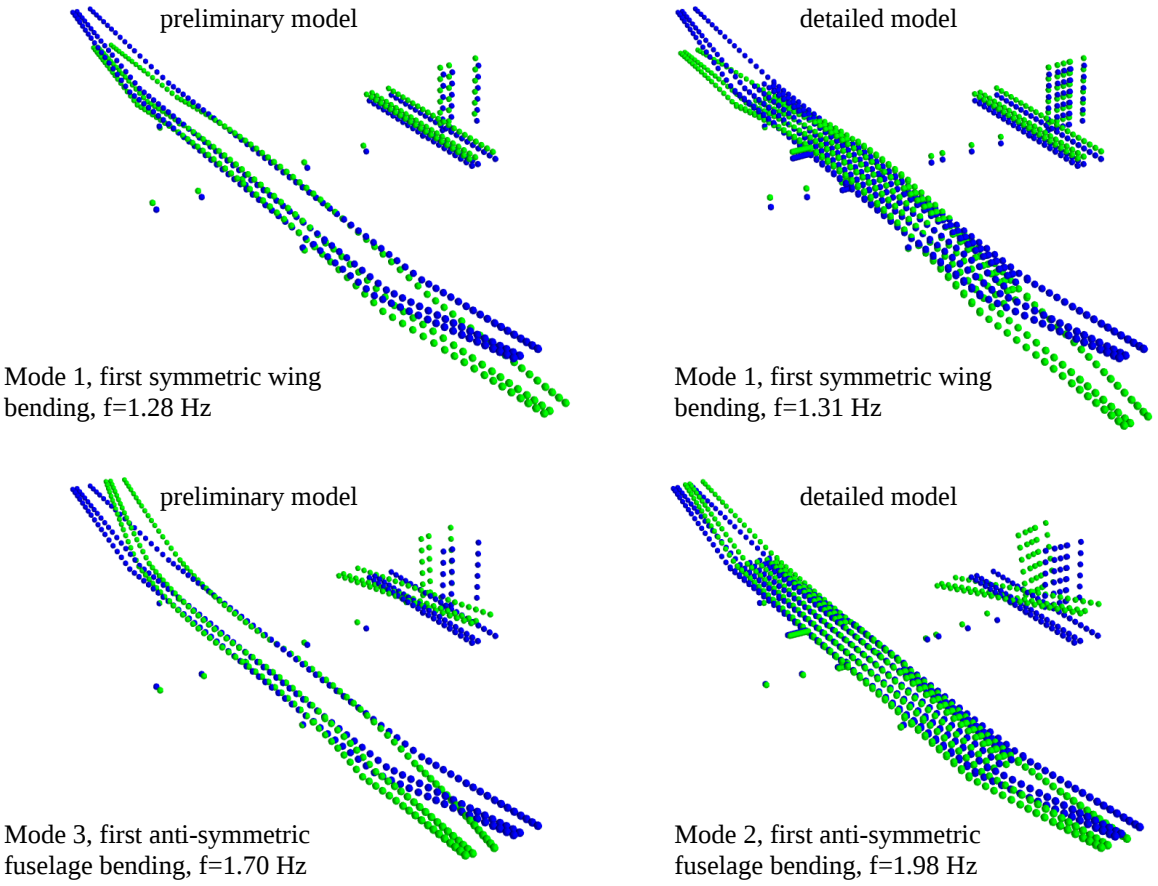


Figure 5: First flexible mode shapes and frequencies, left: preliminary model, right: detailed model

### 2.4 Aerodynamic Modeling

The design maneuvering speed VA is 9.1 m/s EAS with a stall speed VS at 6.5 m/s EAS and a maximum cruise speed VC of 11.0 m/s EAS. The altitude ranges from sea level up to 25.0 km, as the aircraft is supposed to fly most of the time above the regular air traffic, except for climb and descent phases. The airfoils of the wing (MH169 airfoil family) are custom designed by the DLR Institute of Aerodynamics and Flow Technology to deliver optimal performance under these operational conditions. Both Reynolds (typical range Re = 150,000 … 1,000,000) and Mach numbers (up to Ma = 0.3) are moderate and well within the subsonic regime. Thus, aerodynamic panel methods such as the steady vortex lattice method (VLM), the unsteady doublet lattice method (DLM) or the steady/unsteady ZONA6 method yield an acceptable representation of the lifting surfaces. All lifting surfaces (wing, horizontal and vertical tail) are modeled, resulting in an aerodynamic panel mesh shown in Figure 6 on the left. The aerodynamic panels are corrected for airfoil camber, geometrical pre-twist along the wing-span, and an angle of incidence. A full documentation of the implementation, the equations involved as well as a validation of the resulting pressure distributions is given in a technical report by Voß [14]. For the detailed flutter analyses in Section 4.1, a ZONA6 panel mesh is set-up, shown in Figure 6 on the right, which includes the fuselage but no camber and twist correction is needed. As the planform remains unchanged, there are no adjustments to the aerodynamic modeling for the more detailed design.

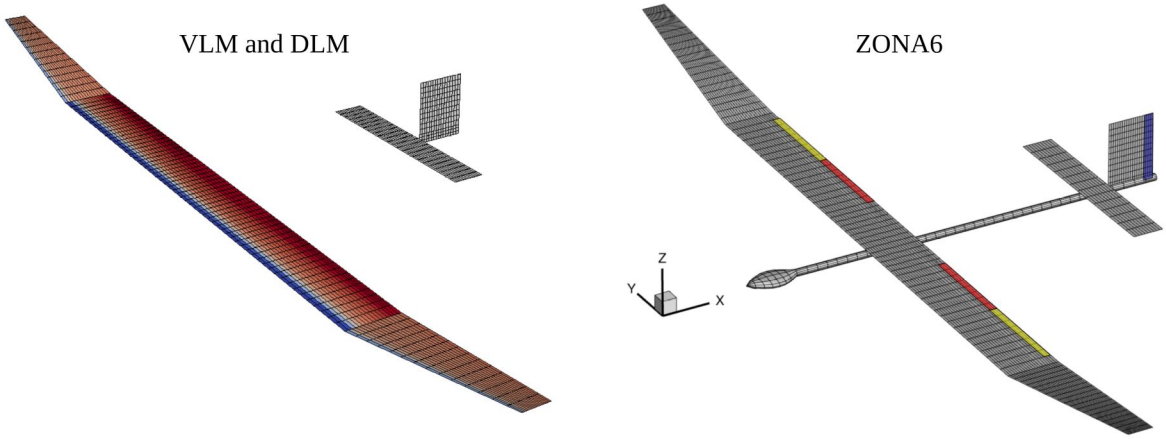


Figure 6: Left: VLM and DLM aerodynamic model, colored by camber and twist correction, Right: ZONA6 aerodynamic model for detailed flutter analyses

### 2.5 Flight Mechanical Interaction and Flight Control System

The flight mechanical motion of the free-flying aircraft is included in the equations of motion following Waszak, Schmidt and Buttrill [2,18,19]. This is important because the aircraft shows a significant rigid body reaction to a gust encounter. It also implies a treatment in the time domain to capture the nonlinear motion as well as the interaction with the flight control system. A publication about the flight mechanical analyses of the HAP aircraft is presented by Hasan et al. [4,5]. A main difference between the flight mechanical and the aeroelastic model is the aerodynamic approach and the way elasticity is included. The aerodynamic data for flight mechanical simulations is typically more detailed and includes more aerodynamic effects (e.g. drag, roll-yaw-coupling, etc.), but is given in terms of global coefficients while the VLM and DLM used in this work calculate a pressure distribution, which is a pre-requisite for loads and aero-structural coupling. Summing up, this work includes flight mechanical effects but does not replace a dedicated flight mechanical analysis.

The aircraft possesses a flight control system, which is prepared by the DLR Institute of System Dynamics and Control. The selected flight control system architecture is depicted in Figure 7. From left to right (or outer to inner), the command signals are

- Flight Management System (FMS): World Geodetic System (WGS) longitude, latitude and altitude $[\lambda \quad \mu \quad h]^T$.
- Outer loop: flight path angle, calibrated airspeed, ground track angle, cross track error $[\gamma \quad V_{\mathrm{cas}} \quad \chi \quad \Delta y]^T$.
- Inner loop: bank & pitch attitude, lateral acceleration $[\Phi \quad \Theta \quad n_{\mathrm{y}}]^T$.
- Control allocation: moment demands in roll, pitch and yaw.

For the closed-loop gust load analyses in Section 3, the outer loop and the FMS are neglected, as they are designed for low frequency guidance tasks (bandwidth < 0.1 Hz). This is less than 10% of the first flexible mode's frequency (compare to Figure 5), which backs the assumption that the outer loop is not relevant for the loads analysis. For tuning of the control laws, the aeroelastic model described in Sections 2.1 to 2.4 is used and augmented with a drag polar in order to account for some of the flight mechanical effects which are not included in the

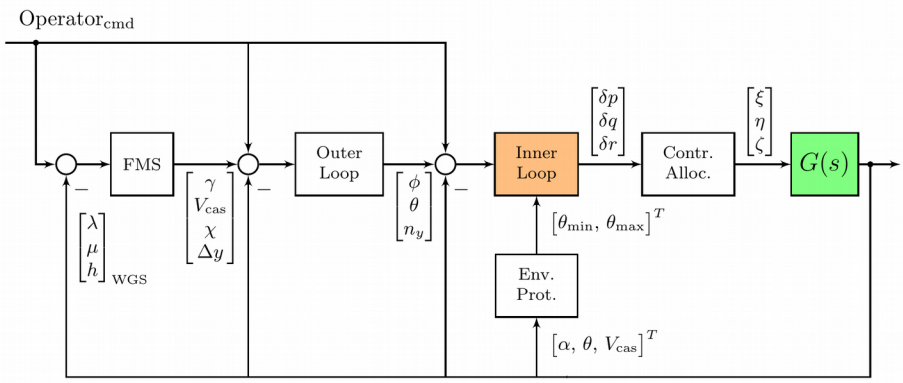


Figure 7: Architecture of the proposed flight control system

aeroelastic model. From the preliminary design to the current stage, the controller was revised and optimized multiple times [20].

## 3 LOADS ANALYSIS AND STRUCTURAL SIZING

### 3.1 Load Cases

The velocities and altitudes considered for the aircraft design are shown in Figure 8 and each dot marks one operating point. The airspeeds considered in loads analyses are primarily VS, VA, VC and VNE. Velocities $VO_{min}$ and $VO_{max}$ indicate the nominal operational range. Velocity Vx is used as an additional sample point in the subsequent aeroelastic analyses to bridge the gap between VC and VNE due to the comparatively large difference in dynamic pressure. An overview of the types and numbers of load cases is given in Table 1. For maneuver loads, 15 different vertical maneuvers, 24 different roll maneuvers and six different yaw maneuvers are considered. Application to the different altitudes, flight speeds and mass configurations leads to a total number of 1260 maneuver load cases. Note that not all maneuvers are performed at each operational point, for example there is no pull-up at VS. Discrete gusts of 1-cos type are simulated with seven different gust gradient ranging from $H = 5 \ldots 61\ m$. The aircraft encounters both positive and negative gusts in vertical and horizontal direction as well as orthogonal to the outer wings, leading to a total number of 2016 gust load cases. Because of the variety in flight speeds and gust gradients, the simulated time ranges from 1 to 20 seconds. The maneuver and gust load cases are complemented by four different landing scenarios, where the landing impact from the landing skids is simulated. In addition, there are 54 propulsion load cases, where the engine torque and gyroscopic loads of the two propellers are calculated at different engine operating points.

### 3.2 Loads Software and Quality Control

Several steps are taken to ensure high quality and reliable results. In a first step, the loads process itself is certified according to DIN EN ISO 9001:2015 and described in a quality management handbook. In addition to that, the aeroelastic models are version controlled in a repository. In that way, changes are documented, unintentional changes are more difficult and all modifications are traceable, which is an important aspect when performing simulations repeatedly over a longer period of time, e.g. from preliminary to detailed design as demonstrated in this work.

The software (Loads Kernel [14,15]) is version controlled as well, including mechanisms for continuous quality control. This is important because the software evolves constantly and the latest version must produce the same results compared to the beginning of the project.

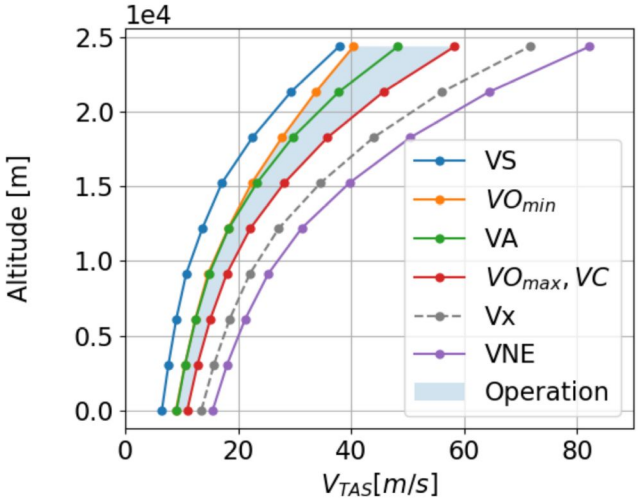


Figure 8: Proposed Design Speeds

| Description | Number |
|---|---|
| Operational points | |
| Altitudes | 9 |
| Speeds | 4 |
| Mass configurations | 2 |
| Vertical maneuvers | 15 |
| Roll maneuvers | 24 |
| Yaw maneuvers | 6 |
| Total Maneuver load cases | 1260 |
| Gust gradients | 7 |
| Gust directions | 8 |
| Total gust load cases | 2016 |
| Approach speeds | 2 |
| Sink rates | 2 |
| Total landing load cases | 4 |
| Engine operational points | 6 |
| Total propulsion load cases | 54 |

Table 1: Overview of type and number of load cases considered.

### 3.3 Load Envelopes

The resulting nodal loads are integrated at so-called monitoring stations, for example along the wing, to create section loads. For the wing, interesting quantities are for example the shear force $F_z$, bending moment $M_x$ or torsional moment $M_y$. For dynamic loads, time slices are used, allowing to merge for example maneuver loads, which are calculated as trim cases, and gust loads.

Figure 9 shows the envelope of the bending moment $M_x$ along the wing span and each dot marks the highest positive or negative bending moment at one monitoring station. Comparing left- and right-hand side, the bending moments are symmetrical with swapped signs because the x-axis of the coordinate system points rearwards for both sides (global coordinate system). Comparing the preliminary with the detailed model, the results are very similar in both shape and amplitude. Small difference can be seen when looking at the corresponding load cases. At the right inner wing, the largest positive bending moment is caused by the 0° (upward) gust at VC at FL600 but with a different gust length (20m vs. 15m). Note that the change of gust length can be partially explained by the selection of discrete gust lengths H = 5, 9, 15, 20, … 61 m, which implies no intermediate steps. The corresponding gust frequency calculated from the gust length and the flight speed has decrease slightly from 1.1 Hz for the preliminary

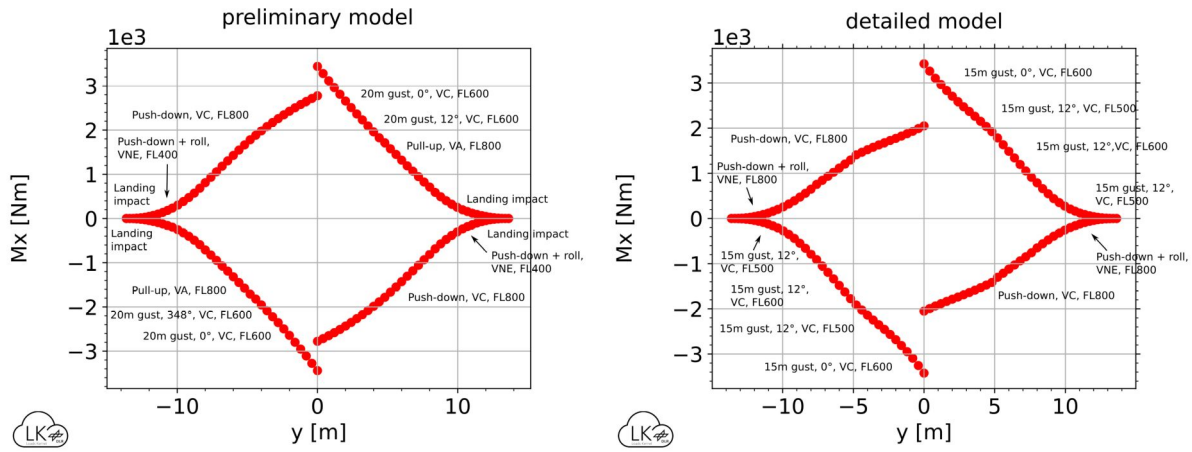


Figure 9: Bending moment $M_x$ along the wing

model to 0.85 Hz for the detailed model. For elastic aircraft, high bending moments typically occur when the gust frequency is close to the first wing bending frequency, which is at 1.3 Hz (in vacuum, compare with Figure 5) for this aircraft. Considering that the eigenfrequencies typically drop with increasing speed and that the flight control system interacts with the gust, these results are plausible. Moving further outboard, the 12° gust at VC, which is orthogonal to the outer wing, causes largest positive bending moments, again at a different gust length (20m vs. 15m). In the detailed model, the pull-up maneuver at VA and FL800 is no longer relevant for the bending moments and the entire wing is dominated by gust loads. However, the maneuver loads are only slightly lower, so that for example a gust load reduction would not yield a large benefit.

At the wing tip, both positive and negative bending moments were caused by the landing impact in the preliminary model, which can be explained by the sudden (de-)accelerations of the aircraft in vertical direction when the skid touches the ground in combination with the structural dynamic reaction. More detailed analyses of the landing phase by the DLR Institute of Flight Systems lead to a reduction of the maximal descent speed from 1.0 m/s to 0.7 m/s for a hard landing. As a consequence, the landing impact no longer dominates the bending moments at the outer wing.

The highest negative bending moments are due to the push-down maneuver at VC and FL800 for most parts of the inner and middle wing, with a combined push-down and roll maneuver at VNE showing up at a few monitoring stations at the outer wing. This can be explained by the nose-down wing torsion due to the $C_{my,0}$ of the airfoil, which is highest at VNE (max. $q_\infty$), plus the additional nose-down torsion due to a downward aileron deflection, which causes negative lift at the outer wing.

Another small difference is a higher engine mass (located at y = 4.8 m) in the detailed model, which is reflected in the bending moments by a small kink at y = 4.8 m while the curve is smoother in the preliminary model.

The torsional moment $M_y$ along the wing span is shown in Figure 10 and the corresponding load cases are more diverse compared to the bending moment $M_x$. The y-axis of the coordinate system points towards the right for both sides (global coordinate system), so that a negative sign indicates a nose-down torsional moment for both side, too. The most obvious difference between the preliminary and the detailed model are the jumps in $M_y$ at y=4.8 and

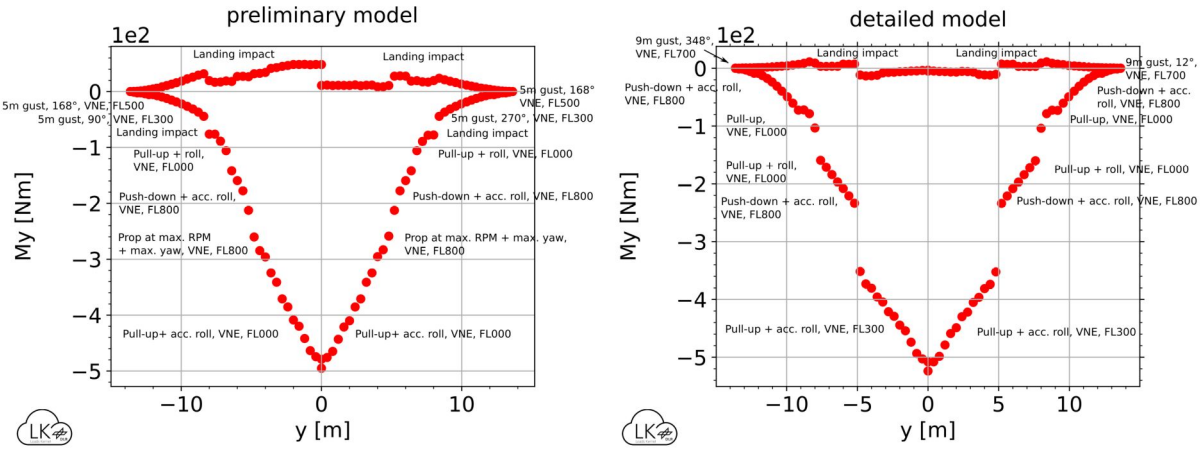


Figure 10: Torsional moment $M_y$ along the wing

y=7.6m. As described in Section 2, the ailerons are now modeled in more detail, including the hinges, but because the aileron attachment is over-determined, the load path is not clear. In a conservative approach, the loading from the two ailerons are added a once to the monitoring stations of the main wing, leading to two distinct jumps in the torsional moment $M_y$.

For most parts of the wing, the highest negative torsional moments $M_y$ are caused by a pull-up maneuver during roll combined with a roll acceleration in opposite direction (e.g. $+p, -\dot{p}$ and vice versa), which can be explained by considering three different effects. First, as already mentioned above, the $C_{my,0}$ of the cambered airfoil introduces a nose-down torsional moment, which is largest at VNE. Second, a downward aileron deflection leads to an additional torsional moment and third, the engine mass mounted on a pylon in front of the wing introduces a torsional moment if exposed to a positive vertical acceleration from both pull-up and accelerated roll. All three effects create torsional moments acting in the same direction.

In the mid-wing area, the gyroscopic loads from the propeller showed up in the preliminary model, while in the detailed model, the rotational inertia of the propeller is reduced from a very conservative approximation (rotating bar) to a more physical value derived from the actual shape of the propeller (more mass close to the hub).

In the outer wing area, several different load cases are identified, most of them just for a few monitoring stations. The highest positive torsional moments are all caused by the landing impact, which excites an in-plane bending motion of the wing, leading to a bending-torsion-coupling due to the out-of-plane masses. Because both the landing simulations and the structural dynamic properties are not perfectly symmetrical, the aircraft tipped to one side in the preliminary model and the results are unsymmetrical as well. Although this is interesting from an academic perspective, the positive values are about one order of magnitude smaller than the negative values and not important for the structural sizing.

### 3.4 Structural Sizing

For the preliminary sizing process of the structural elements, an algorithm based on analytical methods is used. With a beam model (Bernoulli theory) and section loads derived from the load analysis, the primary structural elements are sized, such as wing and tail spars and the longerons (fuselage, pylons), see Figure 11. The masses of other elements like ribs, wing

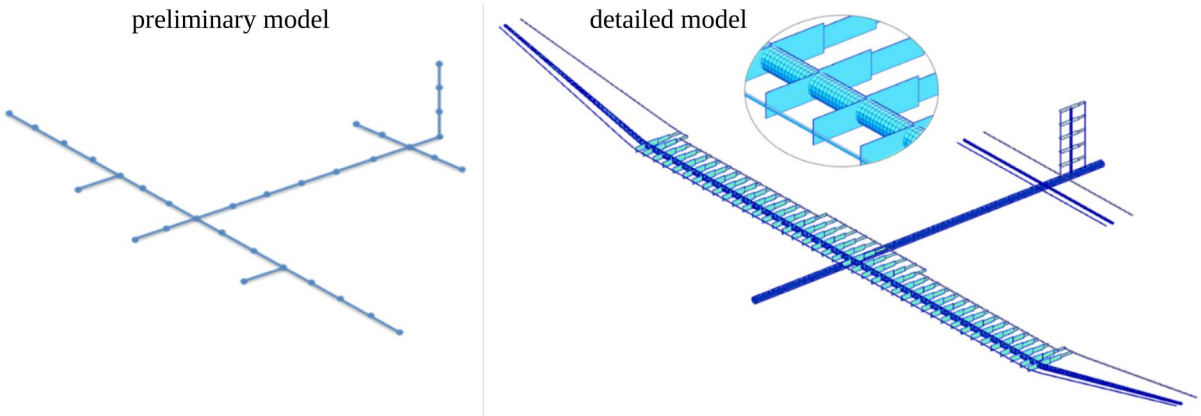


Figure 11: Analytical beam model and global finite element model (GFEM) for structural sizing

covering including solar generator or joining elements are scaled volumetrically or two-dimensionally, which is an adequate approach for the preliminary design. The sizing criteria of the beam elements are material strength, stability and torsional and bending stiffness demands. For instance, for the spars, the design parameters are material thickness, tube diameter, rib or frame spacing and material parameters (laminate stacking). As material model, a smeared wound laminate is assumed, so that thickness is the only design parameter, and different laminates with smeared stiffness and strength properties are considered. A minimum material thickness prevents non-manufacturable wall thicknesses. Detailed finite element models are created to verify the design and mass estimation of particularly critical elements/areas (such as bonded connections, rib scaling, wing-fuselage-joint).

In the more detailed design phase, this sizing model is extended / replaced by a global finite element model (GFEM) of the full aircraft, see Figure 11. The load-bearing primary structure consists of composite shell elements, which are used to model the orthotropic material behavior and to evaluate the stresses in each layer of the laminate. The analytical model is still used to extract the most critical load cases out of the load case envelope (over 300 load cases) as the calculation time is multiple times lower than for the GFEM. To verify different design

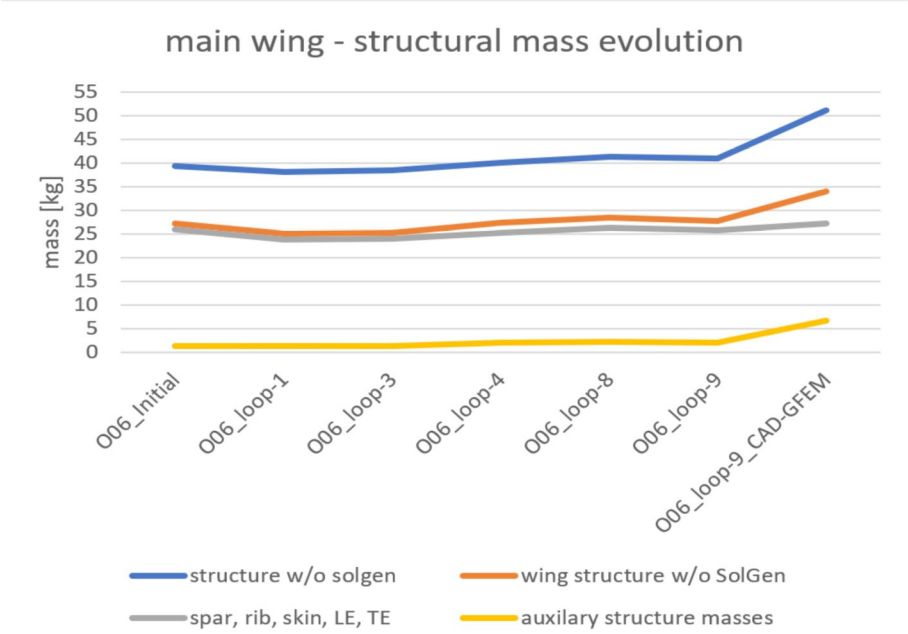


Figure 12: Structural mass evolution

options in an iterative process, a parametric approach to build the GFEM is chosen. The method (to build the model) is based on property IDs, which enables a straightforward way to create individual element sections, i.e. spar segments. In this way, different laminate stackings (PCOMP and MAT8 cards) can be assigned to the individual element sections. Instead of section loads like in the analytical model, now the nodal loads are applied directly to the GFEM (via FORCE and MOMENT cards) after a multiplication by the ultimate design load factor. In order to transfer the nodal loads e.g. from the rib nodes to the main spar, beam elements are added to the GFEM. Thus, the GFEM looks similar to the aeroelastic FE model (compare with Figure 3), but has a more detailed modeling (beam vs. shell elements), which are required for the sizing but not for aeroelastic purposes. For the strength analysis, the Hashin failure criterion [6] is chosen to verify the strength for each layer of the laminate. The stability of the structure is tested in a separate buckling analysis. All failure modes in each element are evaluated automatically and the lowest margins for each load case are exported for interpretation and design adaptation.

In the preliminary design phase, the structural masses remained relatively constant with a slight increase of the structural element masses in the wing (loop-1 to loop-9) as shown in Figure 12. The switch to the detailed GFEM comes along with more detailed mass estimates derived from the CAD-model, so that the mass of the secondary/auxiliary structures increased significantly (yellow line) while the primary structural masses (grey line) show only a slight change. To maintain the target design mass ($m_{\mathrm{design}}$ = 136 kg), batteries are removed. Since both types of masses are in the wing and by distributing them appropriately, the two effects compensate each other so that the load distribution changes only slightly, as shown in the previous section. Auxiliary masses are e.g. additional stiffening ribs, which are needed to maintain the tension in the outer skin, reinforced ribs for load application, overlapping spar sections required for joining individual segments or the transfer of the ideally sized wall thicknesses to explicit, manufacturable laminate stackings. At this point, it should be mentioned that the additional auxiliary masses are a conservative first approach and a reduction of these masses is now the focus of the detailed design phase. More detailed knowledge is expected from the upcoming wing bending test described in Section 5.2.

## 4 AEROELASTIC ANALYSES

Multiple static aeroelastic analyses with respect to jig and flight shapes, control surface effectiveness and longitudinal stability were performed and monitored continuously from the preliminary to the detailed design. The static aeroelastic analyses show no potential problems, more details can be found in Section 4 in [17]. A flutter check was performed at selected operational conditions (at FL000, FL400 and FL800) to reveal and avoid any obvious flutter mechanism already during the preliminary design. In addition, to better investigate the influence of the low-frequency elastic modes on the oscillatory flight mechanical modes, a state space system was set up, see [17]. In this work, the focus is on a more comprehensive flutter analysis based on the more detailed models.

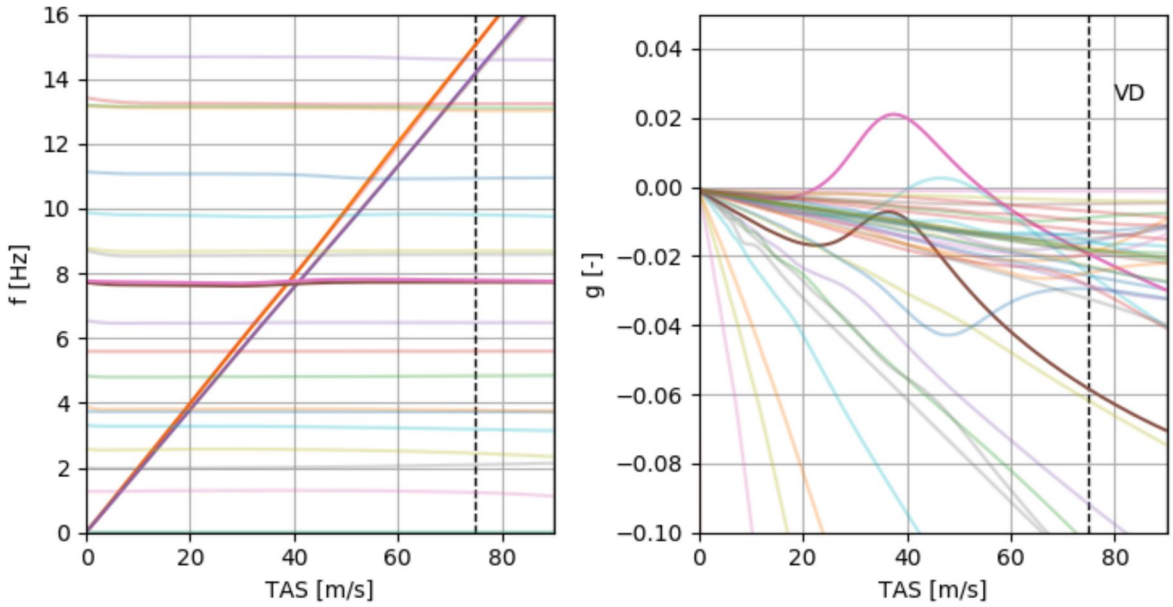


Figure 13: Frequency and damping plot for free-floating control surfaces at 25km flight altitude, the modes involved in the asym. flutter coupling are highlighted

### 4.1 Detailed Flutter Analysis

After the flutter checks during the preliminary design, a more detailed flutter analysis is conducted with the models described in Section 2. Alongside lifting surface flutter such as wing-torsion-flutter, the goal of the more detailed analysis is to cover a broader range of possible instabilities, further de-risking the design with regards to aeroelastic instabilities. Especially couplings of the control surfaces with the lifting surfaces and possible whirl flutter due to the rotating propeller are accounted for.

The detailed flutter analysis is conducted using the in-house software framework PySTAB [8], which is based around the commercial ZAERO-Software [21]. PySTAB allows for several additions to classical frequency-domain flutter models. In this case the addition of unsteady aerodynamic forces caused by the propeller are of major interest to capture possible whirl flutter couplings. The propeller of the HAP aircraft is a two-bladed fixed-pitch propeller. Due to the two-bladed nature it adds periodic aerodynamic and inertial forces to the system, prohibiting a classical eigenvalue-analysis-based flutter analysis. In a first step, time-averaged propeller aerodynamic forces according to the Houbolt/Reed-method [8,11] are used. The effect of periodicity and eventual additional instabilities (such as parametric resonance) due to periodicity will be analyzed in future analyses.

The aerodynamic model used for the flutter analysis is similar to the aerodynamic model presented in Section 2.4 and is shown in Figure 6 on the right. The two main differences are a separate splining of the control surfaces (corresponding panels marked in Figure 6 by yellow, red and blue colors) and a non-lifting body model of the fuselage. Special emphasis is put on the rotational stiffness (torsional springs in Figure 2) of the control surface hinges, modeling the actuation system. A test-based model updating described in Section 5.1 will verify the actuator stiffness but is not (yet) included in the results. Instead, a parameter study is carried out to find possible critical flutter couplings and to understand the sensitivity with respect to this parameter. The propeller forces and torques are applied to the model on the front engine

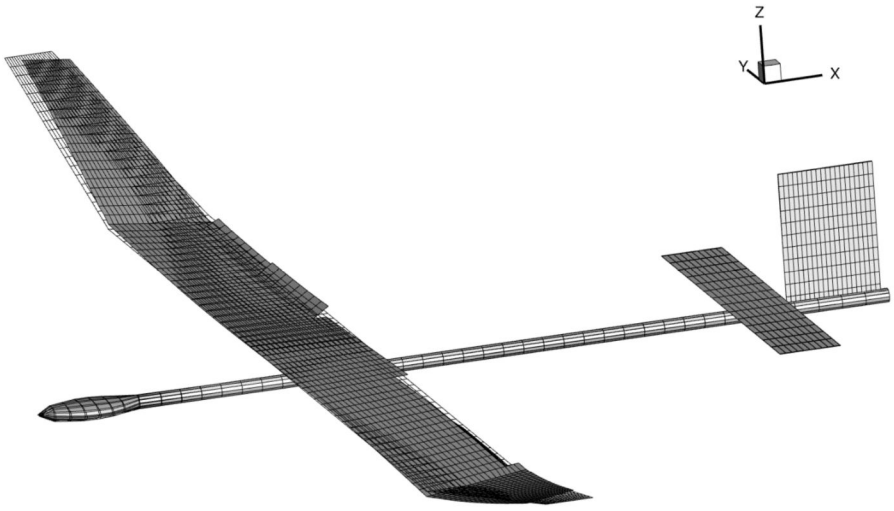


Figure 14: Flutter mode shape of the dominant flutter coupling (from Figure 13) between wing torsion and aileron deflection

pylon, see Figure 2. In the current design no shock mounts between motor and pylon are planned, so the motor is rigidly attached to the pylon.

Figure 13 shows an example result of the flutter assessment. The frequency and damping results for all eigenmodes are shown for a configuration with free-floating control surfaces (e.g. due to actuator failure) at maximum flight altitude of 25 km and with varying true airspeed. This configuration shows two hump-mode-instabilities, the dominating one is highlighted in Figure 13, the corresponding mode shape is shown in Figure 14. As it can be seen from these figures, these instabilities are control-surface-flutter caused by a coupling between the aileron modes and the wing torsion. Couplings like these can be prevented by mass balancing the ailerons and tuning actuator stiffness with the rest of the structure.

Throughout the parameter studies of the actuator stiffness as well as flight altitude, couplings of the ailerons were the only instability found. Especially, no wing-torsion or empennage flutter was found, verifying the result of the flutter checks performed during the preliminary design. Also, no tendency towards whirl flutter was found. Reasons for this are the relatively stiff motor attachment and the large amount of aerodynamic damping due to wing aerodynamics.

## 5 STATIC STRUCTURAL TESTING

Because the detailed models need to be validated, this Section gives an overview on the tests that are currently under preparation. Note that these are only first tests based on the current prototypes and demonstrators. For example, a ground vibration test is planned but not (yet) possible as it requires the complete aircraft.

### 5.1 Ailerons

The aileron demonstrator comprises a wing section, one aileron (length of 2.8 m) and the actuator system. The aileron is attached to the main wing with hinges on the left, in the center and on the right, see Figure 15, and there is one actuator per aileron located in the center. For load application along the trailing edge, wooden sticks are glued on top of every rib. In this

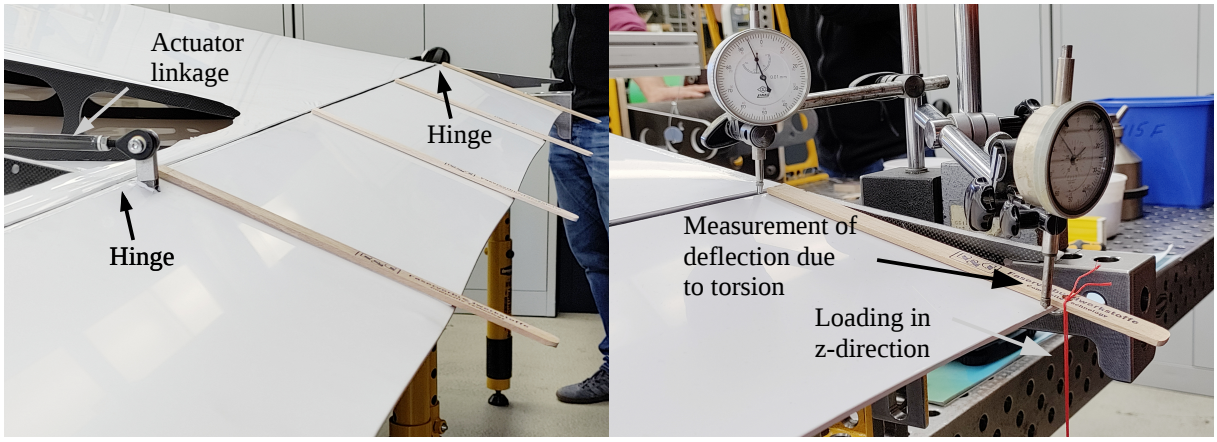


Figure 15: Measurement set-up for aileron torsional stiffness

way, plastic bags with ballast masses from 250 g to 500 g are easily attached using hooks. The following properties are determined in the test:

- aileron mass and center of gravity
- actuator stiffness
- aileron bending and torsional stiffness
- aileron strength

Aileron torsional stiffness: To measure the torsional stiffness, a force in z-direction is applied on each side of the aileron and the deflection of the trailing edge is measured using a micrometer gauge. As a reference, a second gauge is installed at the hinge line.

Aileron strength: For limit load, a maximal torsional moment $M_y \approx 5.5$ Nm is calculated. During the strength test, the aileron is loaded with masses up to 750 g at every rib along the trailing edge, which corresponds to $M_y \approx 11.0$ Nm. The elastic deflection is clearly visible, see Figure 16, and considering a safety factor of 1.5 between limit and ultimate load, the aileron passed the strength test without problems.

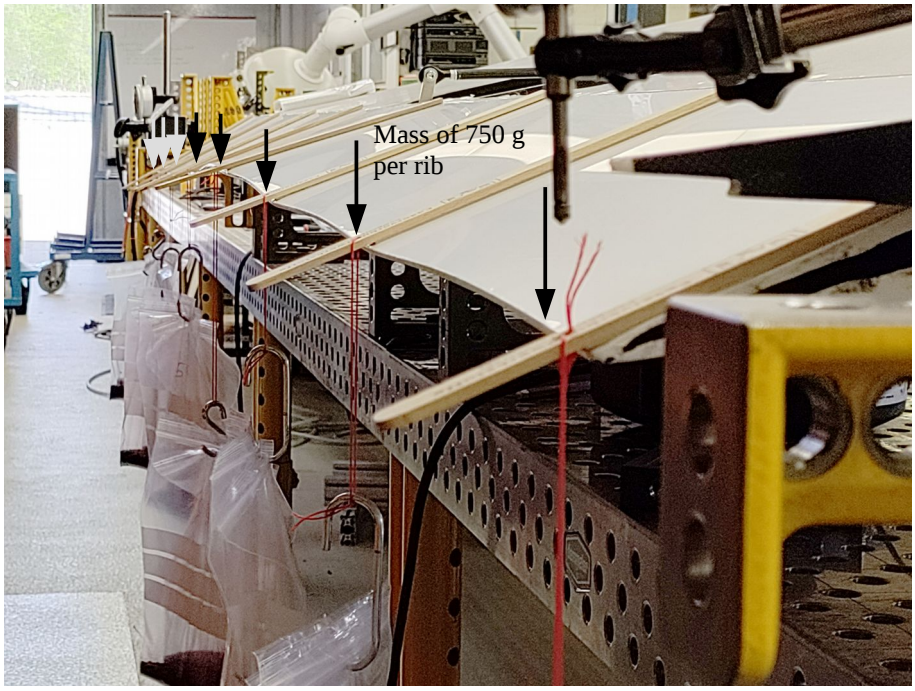


Figure 16: Elastic deflection of the aileron under load

The data obtained during the test is currently processed to update the structural and mass models presented in Section 2.1 and 2.2.

### 5.2 Wing Bending and Torsional Stiffness

Similar to the aileron demonstrator, a complete wing is currently manufactured. The wing structure will be clamped at the wing root and will be subject to single forces and moments (e.g. at the wing tip) as well as load distributions derived from the loads analyses in Section 3.3. Tests are planned to determine the following properties:

- wing mass and center of gravity
- wing bending and torsional stiffness
- wing strength (optional)

The test for wing strength is optional, because the prototype is based on an older design and the test itself is more difficult due to the expected deflections of the wing under ultimate load, which might require a different test rig.

## 6 SUMMARY AND OUTLOOK

In this work, the evolution of the aeroelastic models for a highly flexible, solar electric aircraft from preliminary to a more detailed design is presented. Although many details are added on the modeling side, a comparison of the results obtained from the preliminary and detailed models shows similar structural dynamic characteristics and a similar loading in terms of wing bending and torsional moments $M_x$ and $M_y$. Also, the type of load cases are similar. For the sizing, the analytic approach from the preliminary design is backed-up with numerical analyses using a detailed GFEM model. The analytically sized design is a very good starting point and the transfer to an explicit laminate stacking and spar sectioning can be achieved in few iteration steps. An analysis of the component masses shows only a slight increase in primary structural mass while the secondary/auxiliary structural mass has increased significantly.

A comprehensive flutter analysis based on the detailed models confirms the findings obtained from the flutter checks during the preliminary design. The aircraft itself is free from flutter within the stability envelope, however, control surface flutter could occur in combination with the wing torsional mode. However, tests showed that the actuator provides more stiffness than expected, which indicates that control surface flutter is possibly no issue after all. Future assessments will also include a better propeller model to include the effect of periodicity.

Weight savings are expected for the secondary structural mass once the wing demonstrator has passed the bending test. The aeroelastic models will be updated continuously during the manufacturing process and whenever new test results are obtained. As a final test, a ground vibration test is planned for the complete aircraft. The updated models are the foundation for a flight clearance and the start for flight testing.

## REFERENCES


[1] Benassi, L., and Aquilini, C., “The Structural Dynamics of Flying Non Stop for 100 Days,” in *18th International Forum on Aeroelasticity and Structural Dynamics*, Savannah, Georgia, 2019.

[2] Buttrill, C., Zeiler, T., and Arbuckle, P., “Nonlinear simulation of a flexible aircraft in maneuvering flight,” in *Flight Simulation Technologies Conference, Guidance, Navigation, and Control and Co-located Conferences*, 1987, https://doi.org/10.2514/6.1987-2501.

[3] Gibbs, Y., “NASA Armstrong Fact Sheet: Helios Prototype,” *NASA*, 13-Aug-2015. [Online]. Available: http://www.nasa.gov/centers/armstrong/news/FactSheets/FS-068-DFRC.html. [Accessed: 24-Mar-2017].

[4] Hasan, Y. J., Roeser, M. S., and Voigt, A. E., “Evaluation of the Controllability of a High-Altitude Platform in Atmospheric Disturbances Based on Pilot-in-the-Loop Simulations,” presented at the Deutscher Luft- und Raumfahrtkongress, Online Conference, 2021, https://elib.dlr.de/147221/.

[5] Hasan, Y., Roeser, M., Niemann, S., Hepperle, M., Voß, A., Handojo, V., and Weiser, C., “Flight Mechanical Design and Analysis of a Solar-Powered High-Altitude Platform,” presented at the Deutscher Luft- und Raumfahrtkongress, Online Conference, 2020.

[6] Hashin, Z., “Failure Criteria for Unidirectional Fiber Composites,” *Journal of Applied Mechanics*, vol. 47, no. 2, pp. 329–334, Jun. 1980, https://doi.org/10.1115/1.3153664.

[7] Klimmek, T., “Parameterization of topology and geometry for the multidisciplinary optimization of wing structures,” in *CEAS 2009 - European Air and Space Conference*, Manchester, United Kingdom, 2009.

[8] Koch, C., “Parametric whirl flutter study using different modelling approaches,” *CEAS Aeronaut J*, vol. 13, pp. 57–67, Oct. 2021, https://doi.org/10.1007/s13272-021-00548-0.

[9] QinetiQ, “QinetiQ’s Zephyr UAV exceeds official world record for longest duration unmanned flight,” 10-Sep-2007. [Online]. Available: https://www.qinetiq.com/media/news/releases/Pages/qinetiqs-zephyr-exceeds-world-record.aspx. [Accessed: 24-Mar-2017].

[10] Ritter, M. R., “An extended modal approach for nonlinear aeroelastic simulations of highly flexible aircraft structures,” Doctoral Thesis, TU Berlin, 2019, https://depositonce.tu-berlin.de/handle/11303/9586.

[11] Rodden, W., and Rose, T., “Propeller/nacelle whirl flutter addition to MSC/nastran,” in *Proceedings of the 1989 MSC World User’s Conference*, 1989.

[12] Schwarz, K., “Hochfliegendes UAV: BAE übernimmt PHASA-35-Entwicklung,” 10-Sep-2019. [Online]. Available: https://www.flugrevue.de/militaer/hochfliegendes-uav-bae-uebernimmt-phasa-35-entwicklung/. [Accessed: 15-Nov-2019].

[13] Solar Impulse SA, “Solar Impulse - Around the world to promote clean technologies,” *Solar Impulse*. [Online]. Available: http://www.solarimpulse.com/. [Accessed: 24-Mar-2017].

[14] Voß, A., “An Implementation of the Vortex Lattice and the Doublet Lattice Method,” Institut für Aeroelastik, Deutsches Zentrum für Luft- und Raumfahrt, Göttingen, Germany, Technical Report DLR-IB-AE-GO-2020-137, Oktober 2020, https://elib.dlr.de/136536/.

[15] Voß, A., “Loads Kernel User Guide,” Institut für Aeroelastik, Deutsches Zentrum für Luft- und Raumfahrt, Göttingen, Germany, Technical Report DLR-IB-AE-GO-2020-136, Jul. 2021, https://elib.dlr.de/140268/.

[16] Voß, A., Handojo, V., Weiser, C., and Niemann, S., “Preparation of Loads and Aeroelastic Analyses of a High Altitude, Long Endurance, Solar Electric Aircraft,” presented at the AEC2020 Aerospace Europe Conference, Bordeaux, France, 2020,

https://elib.dlr.de/133496/.
[17] Voß, A., Handojo, V., Weiser, C., and Niemann, S., “Results from Loads and Aeroelastic Analyses of a High Altitude, Long Endurance, Solar Electric Aircraft,” *Journal of Aeroelasticity and Structural Dynamics*, vol. 9, no. 1, pp. 1–22, Jan. 2022, https://doi.org/10.3293/asdj.2021.58.
[18] Waszak, M., Buttrill, C., and Schmidt, D., “Modeling and Model Simplification of Aeroelastic Vehicles: An Overview,” NASA Langley Research Center, NASA Technical Memorandum 107691, Sep. 1992.
[19] Waszak, M. R., and Schmidt, D. K., “Flight dynamics of aeroelastic vehicles,” *Journal of Aircraft*, vol. 25, no. 6, pp. 563–571, Jun. 1988, https://doi.org/10.2514/3.45623.
[20] Weiser, C., and Ossmann, D., “Baseline Flight Control System for High Altitude Long Endurance Aircraft,” presented at the AIAA SCITECH 2022 Forum, 2022, https://doi.org/10.2514/6.2022-1390.
[21] ZONA Technology Inc., *ZAERO: Aeroelastic Design and Analysis*. https://www.zonatech.com/zaero.html.

## COPYRIGHT STATEMENT